Deciphering the Origin of Higher Shell Coordination on Single Iron Catalysts for Resilient Modulating Persulfate Oxidation Into Singlet Oxygen Pathway

ZHANG, Liang, CHENG, Kai, YANG, Zhizhi, ZHANG, Ye, KUBUKI, Shiro, BINGHAM, Paul <http://orcid.org/0000-0001-6017-0798>, YONG, Yang-Chun, ZHANG, Bofan and DUAN, Xiaoguang

Citation:

Copyright and re-use policy

Deciphering the Origin of Higher Shell Coordination on Single Iron Catalysts for Resilient Modulating Persulfate Oxidation Into Singlet Oxygen Pathway

Liang Zhang, Kai Cheng, Zhizhi Yang, Ye Zhang, Shiro Kubuki, Paul A. Bingham, Yang-Chun Yong, Bofan Zhang,* and Xiaoguang Duan*

Precise manipulation of coordination structure of single-atom sites and establishment of schematic microenvironment-oxidation pathway relations remain significant challenges in Fenton-like chemistry. Herein, incorporating sulfur heteroatoms into the higher coordination shell of FeN$_4$ structure (Fe-NSC) exhibited a volcano trend of *p*-hydroxybenzoic acid oxidation, aligning with the number and positions of sulfur dopant. Specifically, higher shell S coordination with moderate electronegativity and larger atomic radii triggers long-range electronic interactions, which provoke Fe 3d orbital splitting and spin electron rearrangement, resulting in a spin crossover with orbital states d$_{xy}$^{2} d$_{yz}$^{1} d$_{xz}$^{2} d$_z$^{21}. As a result, the partial filling of e$_g$ and t$_{2\,g}$ orbitals and moderate σ/π antibonding states between 3d and 2p atomic states optimized the adsorption–desorption behaviors of the key oxygenated intermediates from peroxymonosulfate activation. Thus, the optimal binding configuration weakens the Fe—O bonding and accelerates PMS dissociation to yield C-S-N$_4$Fe-O*, which subsequently couples to form ^{1}O$_2$ with nearly 100% selectivity. The Fe-NSC-functionalized membrane exhibited outstanding long-term reusability in a continuous flow reactor which further validated practical application perspective. This study provides insight at both atomic and electronic levels for rational design of spin-polarized catalysts and its functions in fine-tuning oxidation pathways in environmental catalysis.

1. Introduction

Persistent organic pollution in aquatic environments is a pressing global concern, posing an enormous latent threat to ecosystem safety and thereby to human health. Peroxymonosulfate-based advanced oxidation processes (PMS-AOPs) offer an effective solution by generating reactive oxygen species for pollutant destruction.[1] Sulfate and hydroxyl free radicals (SO$_4$$^{\bullet-}$ and $^\bullet$OH) possess higher redox potentials[2] and prolonged half-lives, facilitating indiscriminate organics oxidation.[3] Nevertheless, these free radicals are vulnerable to environmental factors accompanied by side reactions, which may hinder the desired catalytic behavior.[4,5] Conversely, non-radical reactive species like singlet oxygens (^{1}O$_2$) exhibit appealing characteristics, showcasing strong resistance to background interference, reduced toxic by-products, and improved PMS efficiency, enabling a prospective application in complex pollution treatment.[6]

L. Zhang
School of Environmental and Chemical Engineering
Jiangsu University of Science and Technology
Zhenjiang 212003, P. R. China

K. Cheng, Z. Yang, Y. Zhang, Y.-C. Yong, B. Zhang
School of Environmental and Safety Engineering
Jiangsu University
Zhenjiang 212013, P. R. China
E-mail: bfzhang@ujs.edu.cn

S. Kubuki
Department of Chemistry
Tokyo Metropolitan University
Tokyo 192-0397, Japan

The ORCID identification number(s) for the author(s) of this article can be found under https://doi.org/10.1002/adfm.202417441

P. A. Bingham
College of Business
Technology and Engineering
Sheffield Hallam University
Howard Street, Sheffield S1 1WB, UK

Y.-C. Yong, B. Zhang
School of Emergency Management
Jiangsu University
Zhenjiang 212013, P. R. China

Y.-C. Yong, B. Zhang
Jiangsu Collaborative Innovation Center of Technology and Material of Water Treatment
Suzhou University of Science and Technology
Suzhou 215009, P. R. China

X. Duan
School of Chemical Engineering
The University of Adelaide
Adelaide, SA 5005, Australia
E-mail: xiaoguang.duan@adelaide.edu.au

**ADVANCED
SCIENCE NEWS**

www.advancedsciencenews.com

**ADVANCED
FUNCTIONAL
MATERIALS**

www.afm-journal.de

Consequently, addressing specific wastewater remediation requirements necessitates careful selection or regulation of oxidation pathways by tailoring catalyst properties.

Single-atom catalysts (SACs), featuring highly anchored individual metal atoms on carbon supports, maximize metal site utilization efficiency, overcoming the limitations of traditional homogenous and heterogenous catalysis regarding reaction kinetics and activity.[7,8] Proverbially, the catalytic behavior of SACs is intricately tied to the structure, especially the coordination microenvironment, configuration of metal sites, and the properties of carbon support.[9] The great flexibility in both structure and local chemistry provides tremendous opportunities for fine-tuning SACs to obtain optimal catalytic activity with high selectivity. Owing to the presence of strong metal-support interaction, the variation of physicochemical parameters in carbon support layers also induces significant modulation around the metal sites, thus impacting the catalytic mechanism and capacity.[10] For instance, the electronic density of the state can be substantially increased at the edge of carbon layer compared to its planar counterpart, demonstrating promoted catalytic processes. Moreover, the conjugated sp[2] structures in carbon materials, devoid of unpaired electrons, gave rise to a uniform and conjugated electron dispersion, prohibiting further electronic interactions with metal sites to fine-tune the catalytic behavior of the metal center.[11] Therefore, tailoring the structure and chemistry of the carbon support loaded with single atom sites emerges as an appealing approach to regulating the reaction pathways and performances in PMS-AOPs systems.

The strategic introduction of adjacent coordinative dopants in the first-shell coordination emerges as a promising strategy for optimizing the SACs properties.[12] N-doped carbon matrix is acknowledged as an ideal support for anchoring transition metal atoms, benefiting from robust metal-support interactions. Incorporation of heteroatoms with distinct electronegativities and atomic radii has the potential to disrupt the traditional symmetric architecture of single-atom sites and break the limitation of first-shell coordination via introducing extra dopants or defect configuration in the second or higher coordination shells.[13,14] This results in asymmetric geometry and electron state distribution through weak long-range interactions and electron communications. Moreover, the discrepancy of dopant coordination number and positions may provoke the changes in spin, polarization, and conductivity of the C sp[2] lattice[15] as well as impact the electronic features of the central metal sites.[16,17] Despite the considerable promise of dopant modification in various catalytic systems, including oxygen reduction reaction, hydrogen evolution reaction, and lithium-sulfur batteries,[18–20] establishing the internal and comprehensive association between higher shell coordination, spin electronic theory, and the converted oxidation pathway still requires further enhancement, particularly in PMS-AOPs systems. Crucially, to meet the exact degradation demands of different environments, the intrinsic and microscopic structure-activity correlation of SACs at atomic scale, particularly in regulated portions of radical and nonradical contributions in PMS activation, remains ambiguous and warrants further clear elucidation.

Herein, the underlying catalytic nonradical oxidation pathway of single Fe sites through sulfur incorporation was established. The converted pathway from radicals to $^1O_2$ in Fe-NSC config-

urations was notably influenced by the sulfur doping level and location. Experimental observations and computational analysis revealed that sulfur dopants, with a larger radii, induced high-density defects on the intrinsic carbon matrix, thus broking the distribution symmetry of electronic density and 3d orbital splitting of the Fe sites. Consequently, the modulation induced both spin and electron rearrangement and spin crossover in the e_g orbital, tuning FeN$_4$ sites from $t_{2g}4_{eg}2$ (high spin state) to $t_{2g}4_{eg}1$ (intermediate spin state) upon S doping. The partial filling of e_g and t_{2g} orbitals as typical descriptors and moderate σ/π antibonding states between 3d and 2p atomic states optimized binding energy of Fe site with PMS, weaken Fe—O binding of C-S-N$_4$ Fe-O* intermediate to selectively form $^1O_2$ with significantly reduced energy barriers. This study advances our comprehension of how intricately structured foreign atom modifications impact the regulation of oxidation pathways in SACs-based AOPs catalysis.

2. Results and Discussion

2.1. Synthesis and Structural Analysis of Fe-NC and Fe-NSC Catalysts

Fe-NSC catalysts were synthesized through a successive solvothermal and pyrolysis strategy (Figure S1, Supporting Information). During the solvothermal process, thiourea and formamide served as sulfur and carbon/nitrogen sources, engaging in the Shiff-base reaction to generate dentate polymeric ligand. This ligand could be incorporated into the metal sites. The subsequent high-temperature pyrolysis under a nitrogen atmosphere facilitated the vaporization of zinc compounds and decomposition of organic precursors, resulting in the attainment of highly dispersed single iron metal accommodated in a graphitized carbon layer with sulfur and nitrogen co-doping. High-resolution transmission electron microscopy (HRTEM) depicted the rough surface and no aggregation of particles on the evenly distributed edge flakes (**Figure 1a**). Numerous isolated bright spots with high density dispersed on the carbon layer were clearly observed, without visible particles or clusters detected using high-angle annular dark-field scanning transmission electron microscopy (HAADF-STEM) (Figure 1b). Homogenous dispersion of iron, nitrogen, and sulfur on the carbon matrix was further confirmed through energy dispersive X-ray spectroscopy (EDS) elemental mapping. XRD pattern exhibited only two characteristic broad diffraction peaks $\approx$25 and 44.5° 2θ without specific peaks associated with iron-based compounds for all Fe-NC and Fe-NSC samples, consistent with SCN material (Figure S2, Supporting Information). In Raman spectra, the relatively higher I_D/I_G value of Fe-NSC catalysts (Figure S3, Supporting Information) than Fe-NC signified a defect-rich structure.[21] Further, the crystal dimension along the ab plane was calculated based on the Raman parameters using the following equation: $D_{ab} = (2.4 \times 10^{-10})\lambda_{nm}^4 (\frac{I_G}{I_D})$.[22] The introduction of sulfur evidently shortened the distance of D_{ab}, accompanied by reduced diffusion charge distance and promoted charge transfer capacity.

The possible variation and microenvironment of iron sites were subsequently evaluated. The Fe 2p XPS spectra of Fe-NSC catalyst with "blue shift" after S incorporation implied the lowered chemical valence compared to Fe-NC (Figure 1c). The
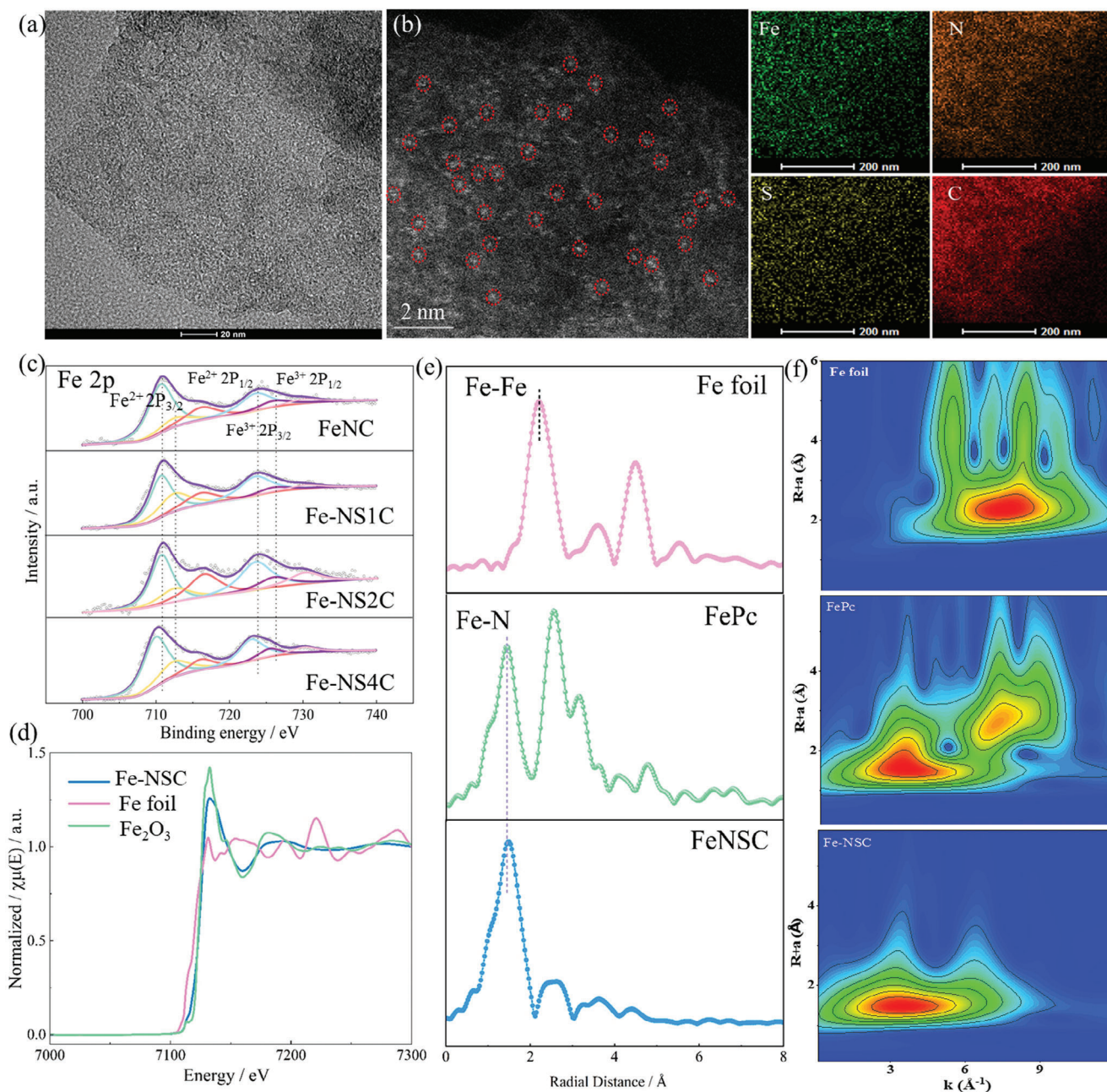
Figure 1. a,b) HRTEM image, HAADF-STEM image and EDS elemental mapping of Fe-NSC catalyst; c) Fe 2p XPS spectra of synthesized catalyst; d) K-edge XANES spectra of sample Fe-NSC, Fe_2O_3, and Fe foil; e) Fourier transforms of the k^3-weighted K-edge EXAFS spectra; f) WT-EXAFS for the Fe element of Fe-NSC, Fe foil, and FePc.

successful modification of Fe-NC by heteroatoms was further confirmed by the S K-edge XAS and S 2p XPS spectra. FT-EXAFS spectrum (Figure S4, Supporting Information) of Fe-NS2C at S K-edge exhibits only one major peak at ≈ 2.0 Å, confirming the scattering S-C path. The characteristic peaks ≈ 161.5 and 163.5 eV were ascribed to S $2p_{3/2}$ and S $2p_{1/2}$ of C-S moieties (Figure S5, Supporting Information). Additionally, the sulfur content in Fe-NS1C, Fe-NS2C, and Fe-NS4C catalysts was measured as 0.74, 1.49, and 2.64 at.%, respectively. No characteristic peak assigned to Fe—S was observed, validating that S is doped onto carbon lay-

ers without directly bonding with iron sites. Further, theoretical calculation was performed to reveal the potential doping location of sulfur on the molecular Fe-N$_4$ moiety, along with the formation energy at different S locations. Figure S6 (Supporting Information) depicted different sulfur locations surrounding the Fe-N$_4$ configuration, designated as M_{S1}, M_{S2}, M_{S3}, M_{S4}, M_{S5}, and M_{S6} based on the number and position with the order of absolute value of formation energy ($M_{S5} > M_{S6} > M_{S4} > M_{S2} > M_{S3} > M_{S1}$), indicating the most likely stable pattern of M_{S5} configuration with the S atoms in higher coordination shell compared to

**ADVANCED
SCIENCE NEWS**

www.advancedsciencenews.com

**ADVANCED
FUNCTIONAL
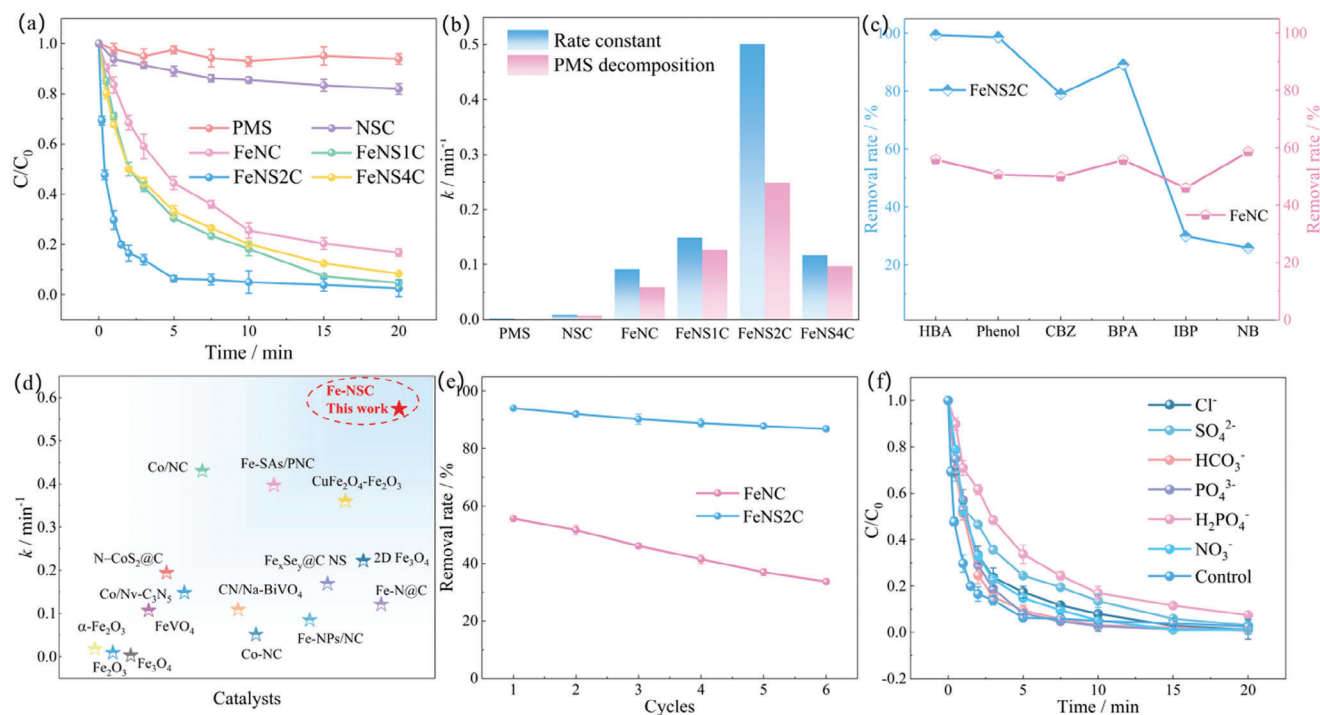MATERIALS**

www.afm-journal.de

Figure 2. a) Catalytic performance of prepared catalysts toward HBA degradation; b) kinetic constants of different systems toward HBA degradation and PMS decomposition; c) comparison of degradation ability of Fe-NC and Fe-NS2C catalysts toward different organic pollutants; d) comparison of kinetic constants using prepared Fe-NSC material with recently reported catalysts; e) sustained degradation of HBA after six cycles in Fe-NC and Fe-NSC systems; f) impact of different anions on HBA degradation efficiency.

the direct bond with iron site as well as second coordination shell. The coordination microenvironment and valence distribution of Fe-NSC were further evaluated. As depicted by Fe K-edge X-ray absorption near-edge structure (XANES) spectra (Figure 1d), Fe-NC and Fe-NSC catalysts are located between the lines of Fe_2O_3 and Fe foil (Fe^0).[23] The absorption edge of Fe in Fe-NSC exhibited a shift to lower energy compared to Fe-NC, consistent with the Fe 2p XPS spectra. The extended X-ray absorption fine structure (EXAFS) for Fe-NSC showed only a broad and strong peak ≈1.5 Å (Figure 1e), assigned to Fe—N in the first coordination shell without Fe—Fe bonding, posing an estimated configuration of FeN_4C with S incorporation in the surrounding N—C matrix,[24] which was consistent with XPS spectra mentioned above. The wavelet transform (WT) EXAFS in Figure 1f was conducted for Fe-NSC catalyst as well as standards (Fe foil and FePc). Compared to characteristic peaks of Fe foil (Fe—Fe) and FePc (Fe—N) in WT-EXAFS, the existence of peak of Fe element in Fe-NSC mainly is assigned to the Fe-N bond, excluding the presence of Fe—Fe bond and establishing an identical atomic M-N moiety with sulfur incorporation in a higher coordination shell.

2.2. Coordination Effects on Catalytic Activity

Hydroxybenzoic acid (HBA), a representative paraben and recalcitrant micropollutant, was chosen as the target pollutant. Adsorption-desorption equilibrium was achieved within 20 min, resulting in ≈25.1% adsorption of HBA (Figure S7a, Supporting Information). No evident HBA removal was observed with individual PMS and NSC (**Figure 2a**). As expected, the simultaneous introduction of PMS and Fe-NSC catalyst remarkably accelerated the catalytic process and improved HBA removal efficiency. Specifically, the activity of PMS activation toward HBA decomposition efficiency increased with the rise of sulfur doping level from Fe-NC (55.7%) and Fe-NS1C (69.6%) to Fe-NS2C (93.7%) but decreased to 66.8% with further S loading (Fe-NS4C). The corresponding pseudo-first-order kinetic rate constants were calculated to be 0.092, 0.149, 0.501, and 0.117 min^{-1}, respectively. Notably, Fe-NS2C surpassed Fe-NS1C and Fe-NS4C by 3.36 and 4.28 times (Figure 2b), revealing a volcano-type trend with increasing sulfur additive levels. Simultaneously, the decomposition efficiency of PMS in different solutions was investigated and presented in Figure 2b and Figure S7b. Fe-NS2C, as the most active catalyst, exhibited the highest PMS decomposition rate (0.249 min^{-1}), significantly outperforming the Fe-NC catalyst (0.059 min^{-1}). Commercial and traditional α-Fe_2O_3, Fe_3O_4, and Fe_2O_3 as well as the previously reported catalysts, were employed as reference catalysts, all of which proved to be inferior to the as-prepared Fe-NS2C catalyst (Figure 2d; Figure S8, Supporting Information). As shown in Figure 2c, Fe-NS2C catalyst showed more superior catalytic capacity than Fe-NC when using HBA, phenol, CBZ, and BPA as target pollutants, while the decontamination efficiencies toward IBP and NB are lower than Fe-NC, implying the selectivity toward specific contaminants. To better evaluate the intrinsic relationship between reactivity and structure properties, the normalized kinetics rate constants ($k_{normalized}$) by catalyst concentration and specific surface area of above heterogenous catalysts were calculated. Obviously, the normalized k value

**ADVANCED
SCIENCE NEWS**

www.advancedsciencenews.com

**ADVANCED
FUNCTIONAL
MATERIALS**

www.afm-journal.de

of Fe-NS2C (0.0062 L m^{-2} min^{-1}) was still 4.66, 3.13, and 4.34 times higher than that Fe-NC (0.00133), Fe-NS1C (0.00198) and Fe-NS4C (0.00143), respectively. Additionally, the turnover frequency (TOF) of each catalyst was calculated via normalizing the reaction kinetics constant by specific iron atom content, wherein the TOF values of Fe-NC, Fe-NS1C, Fe-NS2C, and Fe-NS4C were calculated to be 4.51, 6.25, 21.97, and 6.17 min^{-1} g^{-1}, respectively, further highlighting the significant impact of sulfur doping and position on the activity of single Fe sites. Additionally, the optimal reaction conditions for HBA decomposition including solution pH, catalyst concentration, PMS dosage, initial pollutant content, and water temperature in Fe-NS2C/PMS system were also analyzed and evaluated in detail in Figure S10 (Supporting Information).

Continuous batch experiments were performed to comprehend long-term stability and durability of Fe-NC and Fe-NS2C. Under identical conditions for six consecutive cycles, Fe-NS2C/PMS maintained 92.1% of its original removal efficiency, while Fe-NC/PMS decreased to 40.3% after six cycles (Figure 2e). Different from Fe-NC/PMS system (Figure S11a, Supporting Information) which is vulnerable to water background factors, Fe-NS2C/PMS system exhibited strong resistance to the interferences including anions and cations (Cl$^-$, H$_2$PO$_4^-$, SO$_4^{2-}$, NO$_3^-$, HCO$_3^-$, K$^+$, Na$^+$, and Mg$^+$) (Figure 2f; Figure S11b, Supporting Information). The leachate experiment was performed to evaluate the heterogeneous catalysis effect of Fe-NS2C catalyst. Initially, Fe-NS2C was soaked in an acidic solution and subsequently filtered following HBA degradation to assess the contribution of metal leaching. The filtrate solution contributed only 9.5% HBA removal efficiency, significantly lower than the heterogeneous system (93.7%) (Figure S12a, Supporting Information). Additionally, the leached iron concentration during the catalysis process was measured as 0.32 mg L^{-1} using ICP-OES, accounting for only 0.2% of the catalyst usage with a negligible contribution toward HBA oxidation (Figure S12b, Supporting Information).

2.3. Coordination Microenvironment Effect on ROS Production and Selective Oxidation

To elucidate in detail the generated ROS and unveil the discrepant attack characteristic, electron spin resonance spectroscopy (EPR) was employed using different scavengers including 5,5-dimethyl-1-pyrrolidine-N-oxide (DMPO), DMPO methanol solution, and 2,2,6,6-tetramethylpiperidine (TEMP).[25] In the Fe-NC system, the signal of DMPO-SO$_4^{\bullet-}$/$^\bullet$OH was augmented compared to that of PMS alone, while the introduction of sulfur into the Fe-NSC led to a noticeable decline in the SO$_4^{\bullet-}$/$^\bullet$OH signal (Figure S13, Supporting Information). Intriguingly, the presence of sulfur in the Fe-NSC catalyst markedly improved PMS activation to generate ^{1}O$_2$ (**Figure 3a**). Scavenging experiments involving addition of methanol (MeOH), tert-butanol (TBA), p-benzoquinone (p-BQ), TEMP, and L-histidine to quench SO$_4^{\bullet-}$/$^\bullet$OH, $^\bullet$OH, O$_2^{\bullet-}$ and ^{1}O$_2$, respectively, were also performed. As shown in Figure 3b, the presence of MeOH and TBA marginally hindered the degradation process of Fe-NSC/PMS, whereas the inclusion of TEMP and L-histidine significantly impeded the removal efficiency of HBA, exhibiting a distinct difference from Fe-NC. Both EPR spectra and scaveng-

ing results indicated that the presence of p-BQ did not exert noticeable suppression, and the relatively low intensity of O$_2^{\bullet-}$ precluded the disproportionation pathway of O$_2^{\bullet-}$ to ^{1}O$_2$ (Figure S14, Supporting Information). Conversely, increasing the furfuryl alcohol (FFA) concentration further enhanced the suppression of HBA removal (from 99.3% to 33.4%) (Figure S15, Supporting Information) in Fe-NS2C/PMS system, suggesting the predominant role of ^{1}O$_2$ as the primary ROS in HBA decontamination. The intensity of the TEMP-^{1}O$_2$ signal in EPR spectra steadily increased as the reaction progressed, confirming the continuous production of ^{1}O$_2$ (Figure 3c).

Moreover, various probe compounds, including benzoic acid (BA), nitrobenzene (NB), and FFA, were utilized to explore the steady-state concentrations of SO$_4^{\bullet-}$, $^\bullet$OH, and ^{1}O$_2$, as per the equations provided in Text S6 (Supporting Information). Consequently, the steady-state concentrations of SO$_4^{\bullet-}$, $^\bullet$OH, and ^{1}O$_2$ were computed to be 1.23 × 10^{-13}, 8.38 × 10^{-14}, and 3.86 × 10^{-11} M, respectively, underscoring the prevalence of ^{1}O$_2$ in the Fe-NS2C/PMS system. The relative proportions of ^{1}O$_2$ and free radicals were illustrated in Figure 3d, with the Fe-NS2C/PMS system exhibiting the highest proportion of ^{1}O$_2$, outperforming other catalysts with varying sulfur positions and amounts. Moreover, the results of the kinetic EPR analysis showed continuous ^{1}O$_2$ generation in the Fe-NSC/PMS system (Figure S16, Supporting Information), indicating the crucial role of ^{1}O$_2$ during reaction process. Meanwhile, solvent exchange with D$_2$O instead of H$_2$O accelerated the catalytic performance (96.7% vs 86.2%), attributed to the prolonged lifetime of ^{1}O$_2$ in D$_2$O aqueous system (22–70 μs in D$_2$O system compared to 2.9–4.6 μs in H$_2$O system)[26] (Figure S17a, Supporting Information). A typical mixture of HBA, BPA, and NB pollutants was further employed to ascertain the primary contribution of ^{1}O$_2$. Apparently, the coexistence of NB did not affect the degradation efficiency of HBA and BPA compared to the pristine system (Figure S17b, Supporting Information). NB remained undecomposed due to its higher ionization potential (IP) value and the presence of an electron-withdrawing group, which is only vulnerable to hydroxyl radical, with an ultralow concentration in this work.

The discernible improvement observed with the presence of identical quenchers in the Fe-NC/PMS system implied that sulfur doping not only elevated the catalytic activity but also modulated PMS activation pathway where ^{1}O$_2$ was the dominant reactive species. Undiscovering the origin of ^{1}O$_2$ production is essential to unravel the catalytic mechanism. Generally, there are three pathways for the ^{1}O$_2$ formation during PMS activation[27]: a) transformation of O$_2^{\bullet-}$ from PMS activation to ^{1}O$_2$ through proton-promoted disproportionation; b) SO$_5^{\bullet-}$ (generated from one-electron oxidation of PMS) – mediated ^{1}O$_2$ generation through 2SO$_5^{\bullet-}$ → 2SO$_4^{2-}$ + ^{1}O$_2$ path; c) nucleophilic addition with PMS molecules via surface carbonyl/ketone group to form ^{1}O$_2$. Accordingly, EPR spectra and scavenging results collectively depicted that the presence of p-BQ did not noticeably suppress this process, and the relatively low intensity of O$_2^{\bullet-}$ precluded the disproportionation of O$_2^{\bullet-}$ to ^{1}O$_2$, thus avoiding the Haber-Weiss competitive process.[28,29] No surface carbonyl and ketone groups can be found in synthesized Fe-NSC material via XPS analysis, ruling out nucleophilic addition reactions. Furthermore, the introduction of sodium nitrite, a SO$_5^{\bullet-}$ radical scavenger, did not induce the inhibition of HBA decontamination
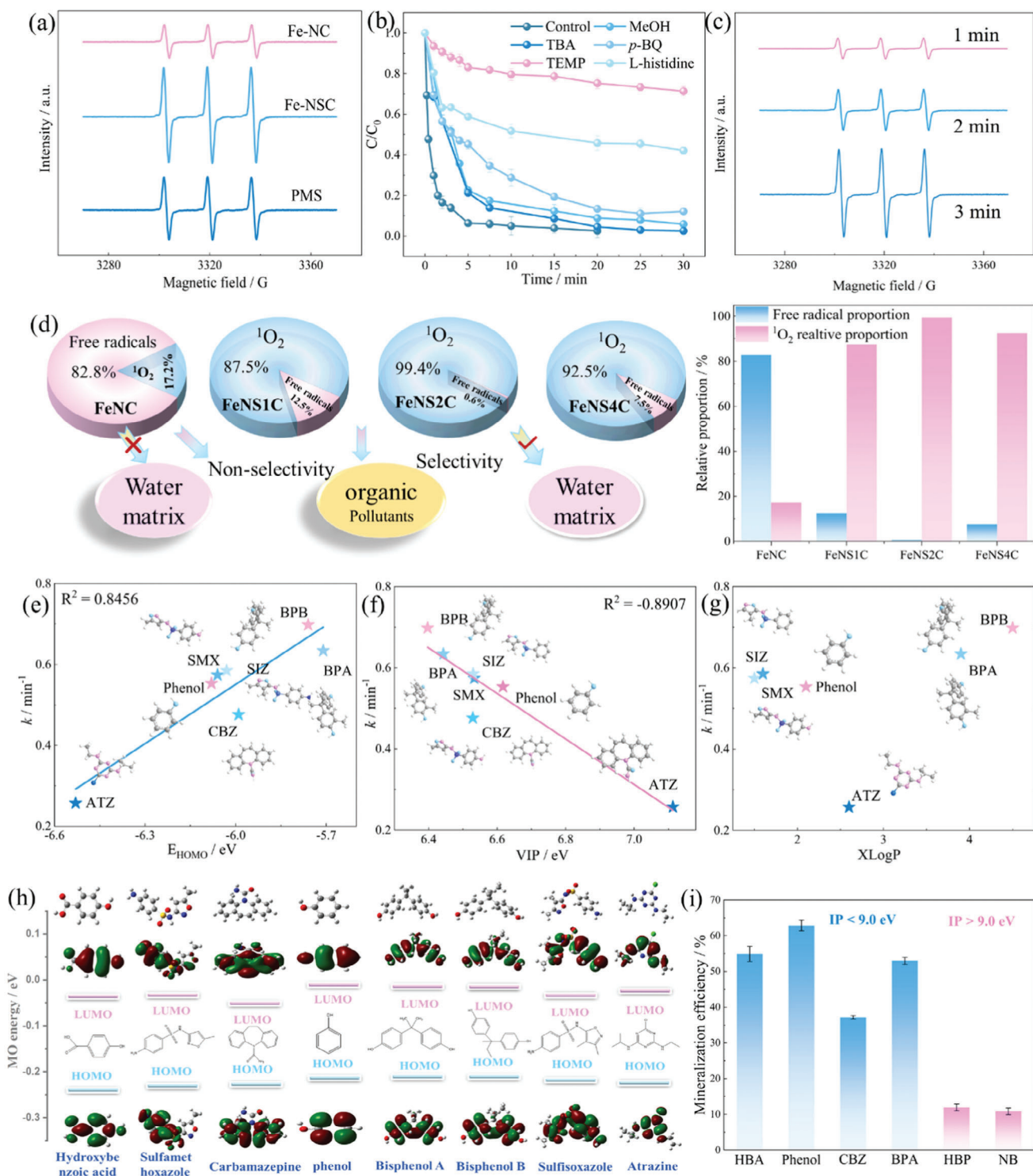
Figure 3. a) EPR spectra of $^1O_2$ under different systems; b) Scavenging experiments in the Fe-NSC/PMS system using different quenchers; c) EPR spectra of $^1O_2$ with the extension of reaction time; d) proportion of nonradical species and free radicals in each system based on the calculated steady-state concentration; e–g) the relationship between catalytic activity and physicochemical properties (VIP, E_{HOMO}, and XLogP); h) the related HOMO, LUMO and HOMO-LUMO gap energy of each organic compound and corresponding structure; i) mineralization efficiency of Fe-NSC/PMS system toward different organic pollutants.

**ADVANCED
SCIENCE NEWS**

www.advancedsciencenews.com

**ADVANCED
FUNCTIONAL
MATERIALS**

www.afm-journal.de

performance (Figure S18, Supporting Information), excluding the role of $SO_5^{\bullet-}$ transformation for $^1O_2$ production. Additionally, N_2 purging did not affect HBA degradation efficiency (Figure S19, Supporting Information), demonstrating that $^1O_2$ did not originate from dissolved oxygen. Thus, it can be inferred that the production of $^1O_2$ mainly stemmed from the direct decomposition of PMS mediated by the single-atom sites. Besides, the possibility of high-valence iron complexes accompanying the oxygen atom transfer pathway was subsequently investigated. Methyl phenyl sulfoxide was used as the probing substrate for high-valence iron, which will undergo oxygen atom transfer pathway and transfer into the corresponding methyl phenyl sulfone with high selectivity. However, the yield of methyl phenyl sulfone in both systems increased by only ≈5% compared to PMS alone (Figure S20, Supporting Information), ruling out the contribution of high-valent iron-oxo complex.

The detailed degradation selectivity toward phenol, bisphenol A (BPA), bisphenol B (BPB), sulfisoxazole (SIZ), sulfamethoxazole (SMX), atrazine (ATZ) and carbamazepine (CBZ) were systematically investigated. The reaction rate constants for each pollutant in Fe-NS2C system followed the order: ATZ < CBZ < Phenol < SMX < SIZ < BPA < BPB. However, deciphering and elucidating the order of catalytic performance solely based on the organic compound's parent parts proves challenging. The removal behavior toward amino groups should theoretically resemble that toward phenolic-based groups due to their similar electron-donating properties. Nevertheless, the catalytic oxidation ability toward CBZ is notably lower compared to BPB and BPA. Considering this, additional structural parameters, including highest/lowest occupied molecular orbital (E_{HOMO}/E_{LUMO}), energy gap (ΔE), vertical ionization potential (VIP), ionization potential, hydrophobic parameter (XLogP), and Fukui function index (f^0/f^-), were chosen for analysis and evaluation, as they are reported to be crucial and indispensable influencing factors in oxidation systems.[30–32] It was observed that the compounds with higher E_{HOMO} values and lower VIP values possessed higher reaction constants, with correlation coefficients of 0.8456 and −0.8907, respectively, in the Fe-NS2C system (Figure 3e–h), in which VIP value emerged as the major factor influencing pollutant catalytic activity, followed by E_{HOMO}. The Fe-NSC/PMS system demonstrated certain electrophilicity and selectivity, tending to extract electrons from specific substances such as carbamazepine compounds. Regarding nonradical pathways, $^1O_2$ with an unoccupied π_{2p} molecular orbital showed highly selective oxidant ability and strong electrophilic capacity.[33] Moreover, TOC removal rate over 37.5% for the organics with IP values lower than 9.0 eV was achieved in Fe-NS2C system, wherein the compounds with higher IP value cannot be efficiently decomposed due to the transformed nonradical species (Figure 3i). Herein, it can be concluded that the highly selective degradation behavior in Fe-NSC/PMS systems stemmed from the converted singlet species with unique attacks toward organics. Additionally, the Fukui function index can reflect the reactivity of the compound molecules, where a higher index represents higher activity of specific sites.[34] Herein, the Fukui index of HBA was calculated (Table S6, Supporting Information), revealing that sites with higher f^- and f^0 were more susceptible to attack by electrophilic species such as radicals and $^1O_2$. Notably, atoms C2, C4, C6, and O8 showed higher f^- values, indicating that the hydroxy and C-H bonds are vulnerable to attack, consistent with the preceding analysis.

2.4. Atomistic Insight into the Origin of Spin Crossover

The interfacial reaction and charge transfer resistance were carried out to explore the modified electronic structure. In Figure S21 (Supporting Information), Fe-NSC exhibited a smaller semicircular diameter than Fe-NC within the high-frequency region in Nyquist plots from EIS measurement, illustrating reduced charge transfer resistance and facilitated electron transfer. Besides, open circuit potential curves depicted a distinct positive potential flow upon PMS injection into Fe-NSC system (Figure S22, Supporting Information), manifesting efficient electron migration from Fe-NSC electrode to PMS through tightly contacted interface. Compared to Fe-NSC, the increased voltage was far lower in Fe-NC system, and the subsequent HBA introduction only triggered slightly negative current flow, collectively validating promoted electron transfer and modified electronic structure.[35] The disparity in atomic radius between sulfur (110 pm) and host nitrogen (65 pm) and carbon (70 pm)[36] may induce atom displacement, lattice strain, and defect formation (Figure S3, Supporting Information), resulting in variation of electronic distribution and local spin density. The higher electronegativity of N (3.04) compared to C (2.55) is beneficial for activating contiguous sp^2-C to carry positive charge and cleaving carbon-π bonds. Although S (2.58) has similar electronegativity yet larger atomic radius than carbon,[34] its doping may provoke local spin polarization and optimize spin state energy levels. This results in an asymmetric distribution of spin-up and spin-down electrons, forming local magnetic moments and promoting spin crossover and spin Hall effect.

To further reveal the impact of sulfur incorporation on electronic distribution, spin-polarized total density of states (TDOS) and partial density of states (PDOS) (**Figure 4**b; Figure S23, Supporting Information) were analyzed. It was indicated that Fe d band center ($\mathcal{E}_d$) shifted upward after sulfur introduction, with an increased PDOS around the Fermi level. This incorporation increased electronic states and shifted the Fermi level, inducing long-range spin polarization and lower spin splitting between low-lying t_{2g} orbitals and high-lying e_g orbitals, which facilitated formation of local magnetic moments and spin state transitions. Correspondingly, pristine Fe-N$_4$C possessed an effective magnetic moment of 1.846 μB, while Fe-NSC decreased (1.691 μB), confirming the spin state transition and spin polarization conversion.[37] The smaller crystal field splitting energy (Δ_0) in intermediate spin state Fe^{II} decreased the energy differences between excited electronic states, facilitating electron transition between t_{2g} orbitals and e_g orbitals (Figure 4a).

To further validate variations in electronic structure and spin states, Mössbauer spectroscopy was employed to probe iron metastable ligand field states and local microstructure. Two essential parameters-center shift (δ, mm s^{-1}) and quadrupole splitting (ΔE_Q, mm s^{-1})-vary among high spin, low spin, and intermediate spin states of Fe^{II} and Fe^{III} ions.[38] All catalysts showed only doublets without sextet or singlet components, excluding presence of iron crystalline species (Figure 4c–f). All spectra could be reliably fitted with three components, indicative
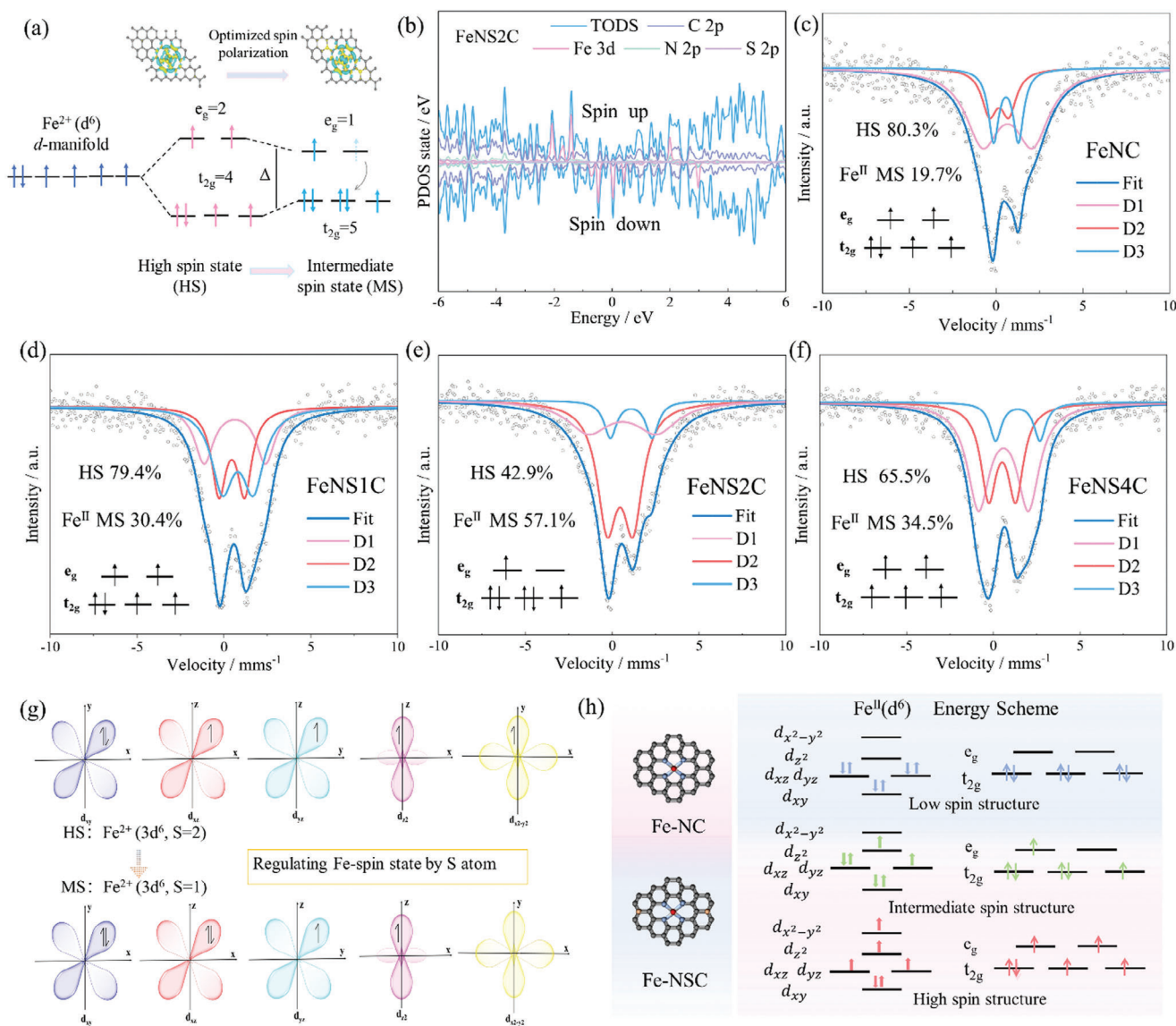
**ADVANCED
SCIENCE NEWS**

www.advancedsciencenews.com

**ADVANCED
FUNCTIONAL
MATERIALS**

www.afm-journal.de

Figure 4. a) The proposed spin state transition process from high spin state to low spin state; b) the PDOS of Fe-NS2C catalyst; c–f) fitted ^{57}Fe Mössbauer spectra of as prepared Fe-NC and Fe-NSC catalysts; g,h) the energy scheme of high spin, intermediate spin and low spin states of iron ions and transformation and orientation of five d orbitals.

of diverse species with varying iron ion valence states and spin states (Table S7, Supporting Information). Notably, with sulfur incorporation, the relative proportion of intermediate spin Fe^{II} moieties ($t_{2g}5e_g2$) follows a volcano-shaped trend as sulfur content increases. Conversely, high spin Fe^{II} ($t_{2g}4e_g2$) moieties progressively decrease, while proportion of high spin Fe^{III} ($t_{2g}3e_g2$) steadily rises. Coordination of central transition metal ion with a switching phenomenon of spin state upon a change in external or intrinsic properties is known as spin crossover[39] The ligand field effect stands as a primary cause of spin state transitions. The degenerate d_{xz} and d_{yz} orbitals along with d_z^2 and $d_{x^2-y^2}$ orbital will be split due to geometric distortion induced by higher coordination shell sulfur incorporation (Figure 4g-h). This electric and ligand field effect increased energy gap between t_{2g} and e_g orbitals, occurrence of coupling between orbital and spin angular

momentum,[40] provoking a redistribution of d orbital energy levels, greater energy splitting, spatial spin electrons rearrangement from high spin ($d_{x^2-y^2} \uparrow d_z^2 \uparrow d_{xz} \uparrow d_{yz} \uparrow d_{xy} \uparrow\downarrow$) into intermediate spin state ($d_z^2 \uparrow d_{xz} \uparrow\downarrow d_{yz} \uparrow d_{xy} \uparrow\downarrow$) with more paired electrons to lower total energy.

2.5. Regulating Oxidation Pathway by Manipulating Spin Electrons and Spin Crossover

Given spin state transitions affecting 3d orbital energy splitting and electron configuration, these changes can provoke σ and π hybridization and alter the adsorption configuration and evolution pathways of PMS intermediates. Consequently, Fe-NSC depicted a higher PMS binding affinity than Fe-NC with adsorption
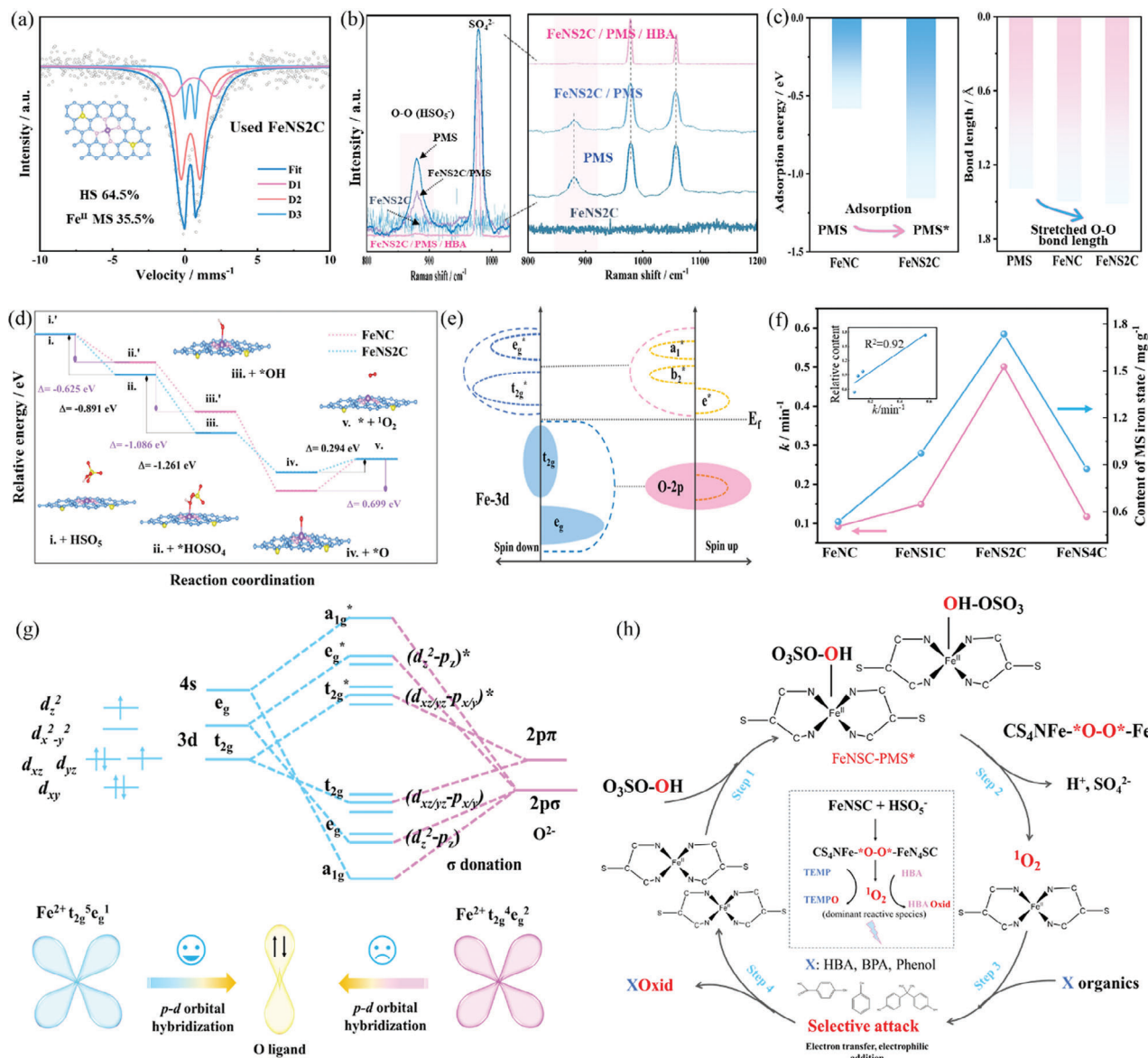
**ADVANCED
SCIENCE NEWS**

www.advancedsciencenews.com

**ADVANCED
FUNCTIONAL
MATERIALS**

www.afm-journal.de

Figure 5. a) Fitted ^{57}Fe Mössbauer spectra of used Fe-NSC catalyst; b) in situ Raman spectra of different systems; c) PMS adsorption energy and O—O bond length in FeNC and FeNSC systems; d) energy profiles for $^1O_2$ evolution pathways in FeNC and FeNSC systems; e) proposed Fe 3d and O 2p orbital interaction analysis of FeNSC; f) correlation ship analysis between catalytic efficiency and intermediate spin state in each catalyst; g) Fe 3d orbital energy level distribution and variation of FeNSC and the hybridization behavior between Fe d-orbital and O p-orbital; h) proposed mechanism of $^1O_2$ catalytic generation in FeNSC system.

energy of −0.581 and −1.155 eV, respectively. Afterwards, O—O bond was also stretched from 1.39 to 1.499, and 1.517 Å for Fe-NC-O(H)OSO$_3^-$ and Fe-NSC-O(H)OSO$_3^-$ (**Figure 5c**). This suggested that induced spin crossover modified electron cloud overlap and charge transfer, especially from Fe d$_z^2$ orbital to p_z orbital of coordinated N via σ bonding in antibonding states,[41] thereby elevating O 2p band center of peroxide bond and elongating O—O bond to $^1O_2$ generation. Subsequently, *in-situ* Raman spectra indicated a gradually decreased I_{1060}/I_{982} value from 0.84 to 0.79 with efficient PMS activation and decomposition (Figure S25, Supporting Information). The addition of Fe-NSC led to a decline of O—O (HSO$_5^-$), nearly vanishing after introducing the HBA pol-

lutant (Figure 5b), implying promoted PMS utilization efficiency, consistent with compatible behavior between PMS consumption and HBA oxidation (Figure S26, Supporting Information).

Owing to higher nucleophilicity of S and modified electronic density of states and Fermi level, it aligned closely with electronic states of PMS and facilitated activation. The d-electrons of intermediate spin-state iron exhibit a mixture of paired and unpaired states, with a spin quantum number (s) lying between high spin and low spin states.[42] Thermodynamic processes for $^1O_2$ generation occurred owing to lower Gibbs free energy than reactant. In Fe-NSC system, empty Fe d$_z^2$ orbital and half-filled d$_{yz}$ orbital in intermediate spin state interact with occupied PMS σ^* and π^*

ADVANCED
SCIENCE NEWS

www.advancedsciencenews.com

ADVANCED
FUNCTIONAL
MATERIALS

www.afm-journal.de

orbitals enabling electrons occupied for O-O cleavage to dissociation of SO_4^{2-} and H^+, forming O*-FeN$_4$SC intermediate, which couples to form a $^1O_2$ and release Fe site (Figure 5e,g,h). Unlike high-valent iron oxo intermediates that involve multi-step electron transfer,[43] the O*-FeN4SC intermediate facilitates $^1O_2$ production. Additionally, high-valent iron oxo intermediates typically exhibit high energy barriers and involve high spin iron sites,[44] maximizing d and p orbitals overlap to form strong Fe=O bonds. In Fe-NC, larger spin angular momentum and occupied lower-energy t_{2g} and e_g orbitals resulted in weak interaction between spin magnetic moment and orbital magnetic moment, leading to stronger spin polarization, spin multiplicity, and electron transfer between Fe 3d and O 2p toward free radicals and high-valent iron species formation. Our previous research also proved this conjecture.[45]

The energy profiles and binding configurations into $^1O_2$ and free radicals are presented in Figure 5d. Notably, the PMS molecule bonded with ≡Fe-N$_4$SC yields a ≡Fe-N$_4$SC-HSO$_5$* complex, which dissociated into H^+ and SO_4^{2-} with generation of O*-FeN$_4$SC. Ultimately, the dissociation of two weakened Fe─O bonds will evolve into $^1O_2$ species, with a total energy barrier of -2.716 kcal mol^{-1}. According to the Sabatier principle, optimal adsorption and desorption energies between the catalyst and reactants should be balanced. The $^1O_2$-derived free energy diagram indicated FeNSC had more favorable thermodynamics for HSO_5^- and desorption of SO_4^{2-} than FeNC. Furthermore, the energy barrier for forming $^1O_2$ from O* is significantly lower ($\Delta = 0.294$ eV) than FeNC ($\Delta = 0.699$ eV), indicating more thermodynamically favorable toward $^1O_2$ production from Fe-centered sites with intermediate spin crossover and oriented ROS production as descriptors of e_g and t_{2g} filling of Fe 3d orbitals.

Subsequently, correlation analysis between spin crossover, reaction rate constant, and $^1O_2$ production proportion was systematically investigated. Comparing catalytic capacity of Fe-NC and Fe-NSC catalysts, the improved kinetic constant closely correlated with relatively larger proportion of intermediate spin polarization ($d_{xz} \uparrow\downarrow d_{z}^2 \uparrow\uparrow d_{yz}$) in Fe-NS2C, with a correlation coefficient R^2 of 0.921 (Figure 5f). Unlike Fe-NS1C and Fe-NS4C, the higher intermediate spin state and lower high spin state in Fe-NS2C provoked more singlet oxygen. The proportion of $^1O_2$ also showed a slight positive correlation with spin state assignment (Figure S28, Supporting Information), implying spin crossover dominant ROS conversion via electronic coordination differentiation in d orbitals and p orbitals and affinity modes. Moreover, ^{57}Fe Mössbauer spectroscopy of used catalyst was measured. Data for fresh and used samples were similarly deconvoluted into three doublets, yet the δ, ΔE_Q, and relative ratio exhibited significant differences (Figure 5a; Table S7, Supporting Information). Comparing parameters revealed a decline in intermediate spin configuration and an increase in Fe^{III} content in the used Fe-NSC catalyst, indicating participation of intermediate spin structure of Fe^{II} and dynamic conversion of Fe^{II}/Fe^{III} and spin crossover.[40] This confirmed the intermediate spin configuration ($d_{xy}^2 d_{yz}^1 d_{xz}^2 d_z^{21}$) with a single d_z^2 electron, moderate e_g filling of Fe 3d states, and spin polarization effect.[46] The coupling of orbital and spin angular momentum is conducive to Fe 3d-O 2p bonding penetration to form singlet oxygen species.

2.6. Scale-Up Decontamination and Disinfection Applicability

To further improve the practicability of this system, pilot device was designed to evaluate the promising separation and purification capacity of Fe-NSC material within a continuous flow-through catalytic reaction system (**Figure 6a–c**) through two different loading catalysts: blocky melamine sponge and commercially available PVDF membrane. The pre-preparation procedures involved immersing prepared melamine sponge into a 500 mL aqueous solution containing 2.5 g Fe-NSC powder, followed by ultrasonication for 60 mins. Subsequently, the resulting catalyst sponge was dried at 120 °C for 6 h for further usage. The Fe-NSC/PVDF membrane was created using a vacuum filtration strategy. During the degradation process, the PMS solution was initially mixed with simulated MB pollutant and collectively pumped into catalytic device tower to trigger the oxidation reaction when PMS/MB solution met with catalyst sponge or membrane. The observed change in color of the simulated MB solution, transitioning from dark blue to nearly colorless in the water outlet beaker, indicated the occurrence of an effective oxidation reaction in both membrane and sponge systems. Subsequently, the mixture containing MB, HBA, phenol, and BPA contaminants was applied into continuous flow-through device, and all the selectivity and removal efficiency of above pollutants can achieve above 80% during long-term and continuous reaction processes. Afterward, various cations and anions including Na^+, K^+, Cl^-, NO_3^-, SO_4^{2-}, Br^- and humic acid, as well as different water quality including deionized water, river water, and tap water and mixed organics were introduced into the contaminant mixture (Figures S29–S31, Supporting Information). It can be observed that the removal efficiencies were almost unaffected even in such a complex system with robust resistance to background matrix, whereas the Fe-NC/PMS system was obviously suppressed. The unique properties and outstanding catalytic behavior of Fe-NSC/PMS can be summarized as follows: i) more efficient PMS decomposition efficiency and oxidant consumption rate comparison to the free radical dominated Fe-NC system; ii) remarkable stability and environmental resistance even under higher coexistence substances (organic contaminants mixed different anions) and complex wastewater matrixes. iii) exceptional universality for oxidation of diverse organic compounds possessing strong electron-donating groups[47] with nearly 100% selectivity and superior conversion rate.

Additionally, the inactivation effect toward pathogenic microorganisms was evaluated (Figure 6f). The number of bacterial colonies on the plates remained abundant in the absence of any catalysts, while the introduction of Fe-NSC resulted in exceptional antibacterial efficiency exceeding 99.9% for Escherichia coli (*E. coli*), with almost no surviving bacteria survived after 60 and 120 min, underscoring the superior antibacterial capabilities. Further, the possible decomposition intermediates and corresponding chronic and acute toxicity toward common hydrobionts in aqueous environments were evaluated using LC-MS measurement and Ecological Structure Activity Relationships.[39] Under the attack of ROS, HBA initially underwent ring-opening reactions, yielding pentanal, 2,4-pentadienoic acid, butyric acid, and 2,3,4-Trihydroxybutanoicacid,[48] which were subsequently broken down into smaller molecules including maleic acid,
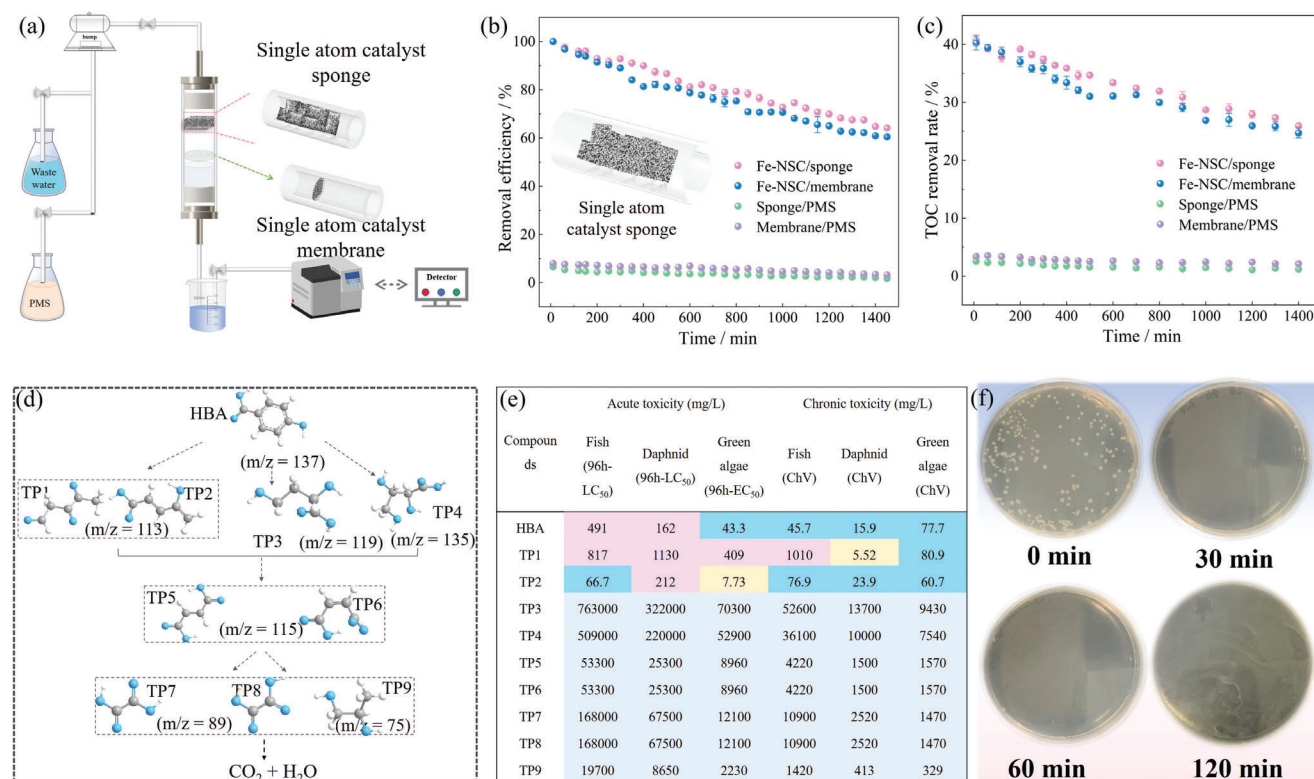
Figure 6. a–c) Schematic illustration of continuous experiments and corresponding treatment performances; d) oxidation pathway of HBA in Fe-NSC system; e) toxicity evaluation of oxidation intermediates of HBA predicted by ECOSAR; f) the antibacterial activity of Fe-NSC material and the resistance performance of Fe-NSC toward different water matrixes.

fumaric acid, oxalic acid, and propanediol.[49] Ultimately, oxalic acid and alcohol experienced additional oxidation steps to culminate in the mineralization of HBA into CO_2 and H_2O (Figure 6d). Additionally, the acute toxicity and development toxicity of HBA and its possible decomposition intermediates were evaluated using Ecological Structure Activity Relationships (ECOSAR) software in Fe-NS2C/PMS system. The acute (LC_{50} and EC_{50}) and chronic ecotoxicity (ChV)[50] of HBA and its possible intermediates on fish, Daphnid, and green algae were presented in Figure 6e, following the Globally Harmonized Standard for the Classification and Labeling of Chemicals. The majority of degradation intermediates depicted significantly lower acute and chronic toxicity compared to maternal HBA molecule and most intermediates were categorized as non-toxicants, reflecting the reduced acute toxicity of HBA after Fenton-like oxidation, which also affirms the efficient oxidation performance and the potential practical sewage application of the Fe-NSC/PMS system.

3. Conclusion

Fine-tuning microenvironmental configuration of single Fe sites, functioning as exemplary heterogenous PMS activators, was accomplished by incorporating heteroatoms into higher shell coordination. This endeavor unraveled the intrinsic relationship between coordination structure, spin crossover, and oxidation pathways. Operando spectroscopy and computational analysis collab-

oratively delineated that long-range interaction, facilitated by heteroatom sulfur doping, effectively activated the iron sites within FeN_4 to realize the ideal one e_g electron ($t_{2g} 4e_g 1$) filling. This, in turn, governed the oxidation route, steering it from free radical to nonradical pathway, thereby allowing superior PMS utilization efficiency and selective generation of $^1O_2$ toward refined organic oxidation capacity. Furthermore, the induced defect state on carbon substrates through S substituting on C sites and spin uncoupling distribution around Fe sites optimized electronic density within the d-band. This fine-tuned interaction strength and bonding state with O 2p in PMS molecule to form the critical intermediate O^*-FeN_4SC, ultimately decreasing the energy barrier for $^1O_2$ formation. In practical application, the sulfur-decorated single-atom system exhibited heightened stability, adaptability, and strengthened resistance to aqueous interference in continuous reaction, presenting promising potential in practical wastewater purification. This work establishes a systematical perspective for rationally designing catalyst coordination structure to precisely regulate ROS generation in PMS-AOPs, shedding light on the underlying internal mechanism, which is invaluable guidance for on-demand converting ROS formation in diverse future environmental applications.

Supporting Information

Supporting Information is available from the Wiley Online Library or from the author.

**ADVANCED
SCIENCE NEWS**

www.advancedsciencenews.com

**ADVANCED
FUNCTIONAL
MATERIALS**

www.afm-journal.de

Conflict of Interest

The authors declare no conflict of interest.

Data Availability Statement

The data that support the findings of this study are available from the corresponding author upon reasonable request.

[1] X. Hu, M. Zhu, *Environ. Sci. Technol.* **2024**, *58*, 10415.

[2] T. Zeng, X. Tang, X. Cai, S. Jin, Y. Zhu, W. Xu, S. Song, H. Zhang, *ACS Catal.* **2024**, *14*, 1405.

[3] Z. Xu, J. Wang, J. Qiu, H. Cao, Y. Xie, *Environ. Sci. Technol.* **2023**, *57*, 14442.

[4] C. Zhang, C. Kong, P. G. Tratnyek, C. Qin, Y. Zhao, Y. Piao, *Environ. Sci. Technol.* **2024**, *58*, 1378.

[5] J. Ye, J. Dai, D. Yang, C. Li, Y. Yan, Y. Wang, *J. Hazard. Mater.* **2022**, *421*, 126715.

[6] Z. Wu, Z. Xiong, W. Liu, R. Liu, X. Feng, B. Huang, X. Wang, Y. Gao, H. Chen, G. Yao, B. Lai, *Environ. Sci. Technol.* **2023**, *57*, 21416.

[7] Y. Zeng, E. Almatrafi, W. Xia, B. Song, W. Xiong, M. Cheng, Z. Wang, Y. Liang, G. Zeng, C. Zhou, *Coord. Chem. Rev.* **2023**, *475*, 214874.

[8] S. Wang, J. Zhang, B. Li, H. Sun, S. Wang, *Energy Fuels* **2021**, *35*, 6504.

[9] Y. Li, H. Sun, L. Ren, K. Sun, L. Gao, X. Jin, Q. Xu, W. Liu, X. Sun, *Angew. Chem., Int. Ed.* **2024**, *63*, 202405334.

[10] W. Tan, S. Xie, D. Le, W. Diao, M. Wang, K.-B. Low, D. Austin, S. Hong, F. Gao, L. Dong, L. Ma, S. N. Ehrlich, T. S. Rahman, F. Liu, *Nat. Commun.* **2022**, *13*, 7070.

[11] S. Liu, J. Du, H. Wang, W. Jia, Y. Wu, P. Qi, S. Zhan, Q. Wu, J. Ma, N. Ren, W.-Q. Guo, *Water Res.* **2024**, *254*, 121417.

[12] Z. Wu, B. Huang, X. Wang, C.-S. He, Y. Liu, Y. Du, W. Liu, Z. Xiong, B. Lai, *Environ. Sci. Technol.* **2023**, *57*, 14046.

[13] Z. Qi, Y. Zhou, R. Guan, Y. Fu, J.-B. Baek, *Adv. Mater.* **2023**, *35*, 2210575.

[14] J. Han, L. Wang, L. Wang, C. Li, Y. Mao, Y. Wang, *Food Chem.* **2019**, *283*, 1.

[15] X. Feng, Y. Bai, M. Liu, Y. Li, H. Yang, X. Wang, C. Wu, *Energy Environ. Sci.* **2021**, *14*, 2036.

[16] X. Liang, N. Fu, S. Yao, Z. Li, Y. Li, *J. Am. Chem. Soc.* **2022**, *144*, 18155.

[17] S. Wang, J. Zhang, B. Li, H. Sun, S. Wang, X. Duan, *J. Environ. Chem. Eng.* **2022**, *10*, 107438.

[18] Y. Wu, Z. Zhuang, C. Chen, J. Li, F. Xiao, C. Chen, *Chem Catal.* **2023**, *3*, 100586.

[19] Y. Zhu, W. Wang, P. Gong, Y. Zhao, Y. Pan, J. Zou, R. Ao, J. Wang, H. Cai, H. Huang, M. Yu, H. Wang, L. Lin, X. Chen, Y. Wu, *ACS Nano* **2023**, *17*, 3064.

[20] Y. Chai, C. Huang, M. Sui, Y. Yin, N. Sun, Y. Chen, Z. Liao, X. Sun, W. Shen, S. Tang, *J. Environ. Manage.* **2023**, *341*, 118079.

[21] M. Couzi, J.-L. Bruneel, D. Talaga, L. Bokobza, *Carbon* **2016**, *107*, 388.

[22] M. Chen, D. Liu, L. Qiao, P. Zhou, J. Feng, K. W. Ng, Q. Liu, S. Wang, H. Pan, *Chem. Eng. J.* **2023**, *461*, 141939.

[23] C. Zhang, Y. Yan, H. Huang, X. Peng, H. Song, J. Ye, L. Shi, *ACS Catal.* **2023**, *13*, 15351.

[24] L. Wang, L. Rao, M. Ran, Q. Shentu, Z. Wu, W. Song, Z. Zhang, H. Li, Y. Yao, W. Lv, M. Xing, *Nat. Commun.* **2023**, *14*, 7841.

[25] Y. Gao, T. Wu, C. Yang, C. Ma, Z. Zhao, Z. Wu, S. Cao, W. Geng, Y. Wang, Y. Yao, Y. Zhang, C. Cheng, *Angew. Chem., Int. Ed.* **2021**, *60*, 22513.

[26] F. Chen, Y.-J. Sun, X.-T. Huang, C.-W. Bai, Z.-Q. Zhang, P.-J. Duan, X.-J. Chen, Q. Yang, H.-Q. Yu, *Proc. Natl. Acad. Sci. USA* **2024**, *121*, 2314396121.

[27] J. Zhen, J. Sun, X. Xu, Z. Wu, W. Song, Y. Ying, S. Liang, L. Miao, J. Cao, W. Lv, C. Song, Y. Yao, M. Xing, *Angew. Chem., Int. Ed.* **2024**, *63*, 202402669.

[28] Q. Yi, J. Ji, B. Shen, C. Dong, J. Liu, J. Zhang, M. Xing, *Environ. Sci. Technol.* **2019**, *53*, 9725.

[29] F. Chen, Y. J. Sun, X. T. Huang, C. W. Bai, Z. Q. Zhang, P. J. Duan, X. J. Chen, Q. Yang, H. Q. Yu, *Proc. Natl. Acad. Sci. USA* **2024**, *121*, 2314396121.

[30] Y. Chai, H. Dai, P. Zhan, Z. Liu, Z. Huang, C. Tan, F. Hu, X. Xu, X. Peng, *J. Hazard. Mater.* **2023**, *452*, 131202.

[31] Z. Chen, F. An, Y. Zhang, Z. Liang, W. Liu, M. Xing, *Proc. Natl. Acad. Sci. USA* **2023**, *120*, 2305933120.

[32] Z.-H. Xie, C.-S. He, H.-Y. Zhou, L.-L. Li, Y. Liu, Y. Du, W. Liu, Y. Mu, B. Lai, *Environ. Sci. Technol.* **2022**, *56*, 8784.

[33] N. Li, J. Ye, H. Dai, P. Shao, L. Liang, L. Kong, B. Yan, G. Chen, X. Duan, *Water Res.* **2023**, *235*, 119926.

[34] S. Li, T. Huang, P. Du, W. Liu, J. Hu, *Water Res.* **2020**, *185*, 116286.

[35] B. Zhang, X. Li, P. A. Bingham, K. Akiyama, S. Kubuki, *Chem. Eng. J.* **2023**, *451*, 138574.

[36] M. Fan, J. Cui, J. Wu, R. Vajtai, D. Sun, P. M. Ajayan, *Small* **2020**, *16*, 1906782.

[37] M. Yu, A. Li, E. Kan, C. Zhan, *ACS Catal.* **2024**, *14*, 6816.

[38] N. N. Greenwood, *Nature* **1965**, *205*, 119.

[39] A. Genoux, M. Pauly, C. L. Rooney, C. Choi, B. Shang, S. McGuigan, M. S. Fataftah, Y. Kayser, S. C. B. Suhr, S. DeBeer, H. Wang, P. A. Maggard, P. L. Holland, *J. Am. Chem. Soc.* **2023**, *145*, 20739.

[40] Y. Wang, P. Meng, Z. Yang, M. Jiang, J. Yang, H. Li, J. Zhang, B. Sun, C. Fu, *Angew. Chem., Int. Ed.* **2023**, *62*, 202304229.

[41] W. Yang, F. Qi, W. An, H. Yu, S. Liu, P. Ma, R. Chen, S. Liu, L.-L. Lou, K. Yu, *ACS Catal.* **2024**, *14*, 5936.

[42] Z. Fang, W. Zhao, T. Shen, D. Qiu, Y. Lv, X. Hou, Y. Hou, *Precis. Chem.* **2023**, *1*, 395.

[43] M. Li, H. Li, C. Ling, H. Shang, H. Wang, S. Zhao, C. Liang, C. Mao, F. Guo, B. Zhou, Z. Ai, L. Zhang, *Proc. Natl. Acad. Sci.* **2023**, *120*, 2304562120.

[44] C. Zhang, N. Ding, Y. Pan, L. Fu, Y. Zhang, *Chin. Chem. Lett.* **2024**, *35*, 109579.

[45] B. Zhang, X. Li, K. Akiyama, P. A. Bingham, S. Kubuki, *Environ. Sci. Technol.* **2022**, *56*, 1321.

[46] X. Zhang, W.-H. Xu, W. Zheng, S.-Q. Su, Y.-B. Huang, Q. Shui, T. Ji, M. Uematsu, Q. Chen, M. Tokunaga, K. Gao, A. Okazawa, S. Kanegawa, S.-Q. Wu, O. Sato, *J. Am. Chem. Soc.* **2023**, *145*, 15647.

**ADVANCED
SCIENCE NEWS**

www.advancedsciencenews.com

**ADVANCED
FUNCTIONAL
MATERIALS**

www.afm-journal.de

[47] P. Yang, Z. Cao, Y. Long, D. Liu, W. Huang, S. Zhan, M. Li, *ACS Catal.* **2023**, *13*, 12414.

[48] R. A. K. Hirani, H. Wu, A. H. Asif, N. Rafique, L. Shi, S. Zhang, Z. Wu, L.-C. Zhang, S. Wang, Y. Yin, M. Saunders, H. Sun, *J. Hazard. Mater.* **2023**, *448*, 130874.

[49] T. Yang, J. Mai, S. Wu, W. Luo, M. Zhu, P. Liang, L. Guo, J. Chen, J. Jia, J. Ma, *Water Res.* **2021**, *205*, 117669.

[50] J. Cao, J. Li, B. Yang, Z. Chen, A. R. Mahjoub, M. Xing, *Cell Rep. Phys. Sci.* **2024**, *5*, 101966.